RSC Advances

ROYAL SOCIETY OF CHEMISTRY

PAPER

View Article Online
View Journal | View Issue

Cite this: *RSC Adv.*, 2020, **10**, 45067

Highly efficient hamburger-like nanostructure of a triadic Ag/Co_3O_4/$BiVO_4$ photoanode for enhanced photoelectrochemical water oxidation†

Xintong Gao,[ab] Zhiqun Bai,[a] Shuai Zhang,[c] Jingchao Liu *[a] and Zenghe Li *[b]

Received 22nd September 2020
Accepted 4th December 2020

DOI: 10.1039/d0ra08102g

rsc.li/rsc-advances

The combination of a semiconductor heterojunction and oxygen evolution cocatalyst (OEC) is an important strategy to improve photoelectrochemical (PEC) water oxidation. Herein, a novel hamburger-like nanostructure of a triadic photoanode composed of $BiVO_4$ nanobulks, Co_3O_4 nanosheets and Ag nanoparticles (NPs), that is, Ag/Co_3O_4/$BiVO_4$, was designed. In our study, an interlaced 2D ultrathin p-type Co_3O_4 OEC layer was introduced onto n-type $BiVO_4$ to form a p–n Co_3O_4/$BiVO_4$ heterojunction with an internal electric field (IEF) in order to facilitate charge transport. Then the modification with Ag NPs can significantly facilitate the separation and transport of photogenerated carriers through the surface plasma resonance (SPR) effect, inhibiting the electron–hole recombination. The resulting Ag/Co_3O_4/$BiVO_4$ photoanodes exhibit largely enhanced PEC water oxidation performance: the photocurrent density of the ternary photoanode reaches up to 1.84 mA cm^{-2} at 1.23 V *vs.* RHE, which is 4.60 times higher than that of the pristine $BiVO_4$ photoanode. The IPCE value is 2.83 times higher than that of the pristine $BiVO_4$ at 400 nm and the onset potential has a significant cathodic shift of 550 mV for the ternary well-constructed photoanode.

1. Introduction

Photoelectrochemical (PEC) water splitting is of great significance to mitigate global environmental problems by converting abundant solar energy into chemical fuels in the form of H_2 or hydrocarbon compounds.[1] The photoanodes have low efficiency compared to the photocathodes since the water oxidation half-reaction occurring in the photoanode is recognized as a speed-limiting step in the overall water splitting reaction. Therefore, it is important to develop an efficient and practical anode system for construction of high-performance PEC cells.[2–4] $BiVO_4$ is a highly promising photoanode, which exhibits proper band gap (~2.4 eV) for solar light absorption and favorable valence band very near the thermodynamic oxygen evolution potential.[5–7] However, poor charge transport, excessive electron–hole recombination, slow hole kinetics of oxygen evolution reaction and limited quantum efficiency are major challenges with the $BiVO_4$ photoanodes.[8,9] To overcome these challenges, various strategies such as elemental doping,[10,11] construction of heterojunctions[12,13] and coupling with various oxygen evolution cocatalysts (OECs)[14–16] have been employed to improve the photoactivity of $BiVO_4$.

Formation of $BiVO_4$-based nanostructured heterojunction photoanodes was recognized as an attractive route to improve PEC water splitting performances because it enlarges the interfacial area, promotes efficient charge separation, and improves the optical absorption.[17–19] Among the rest, staggered (type-II) band structure alignment and complementary solar light harvesting contribute to further improve the PEC property of $BiVO_4$. Especially, p-Co_3O_4 is not only expected to form a p–n junction with n-$BiVO_4$, but also acted as an effective OEC. Thus among the various $BiVO_4$-based heterojunction photoanodes, p–n Co_3O_4/$BiVO_4$ photoanode exhibits the synergetic enhancement of surface reaction kinetics and bulk charge separation. For instance, Wang *et al.* synthesized powdered composite of $BiVO_4$/Co_3O_4 with O_2 evolution of 11 mmol g^{-1} h^{-1}, which is 17 times greater than for unmodified $BiVO_4$.[20] Hou *et al.* also reported Co_3O_4@C/$BiVO_4$ photoanode derived from MOF-template with the enhanced photocurrent density, which is approximately tenfold higher with respect to bare $BiVO_4$.[21]

Although it has been well recognized the surface catalytic effect of Co_3O_4, the modification of Co_3O_4 may introduce more surface recombination centres that hamper the PEC performance inversely, in consideration of the junction formed at the photoanode/OEC interface. In this work, firstly, $BiVO_4$ photoanodes with a nanoporous morphology were synthesized to

[a]State Key Laboratory of Chemical Resource Engineering, Beijing University of Chemical Technology, Beijing 100029, China. E-mail: Jingchaoliu1992@163.com
[b]Key Laboratory of Environmentally Harmful Chemical Analysis, College of Chemistry, Beijing University of Chemical Technology, Beijing, 100029, China. E-mail: lizh@mail.buct.edu.cn
[c]Key Laboratory of Photochemical Conversion and Optoelectronic Materials, Technical Institute of Physics and Chemistry, Chinese Academy of Sciences, Beijing, 100190, China

† Electronic supplementary information (ESI) available. See DOI: 10.1039/d0ra08102g

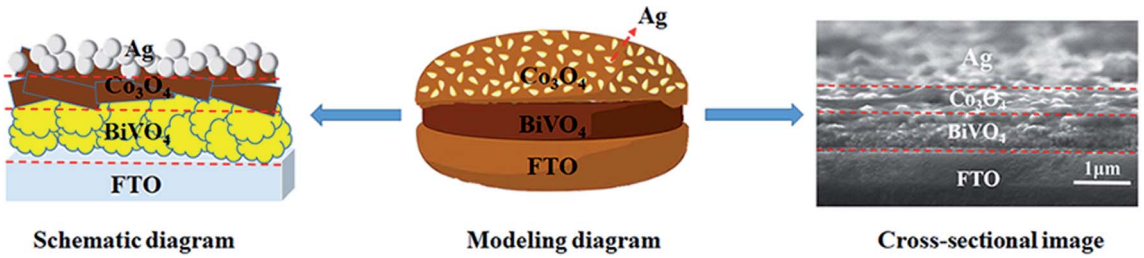

Fig. 1 Schematic diagram, modeling diagram and cross-sectional image of triadic $Ag/Co_3O_4/BiVO_4$ photoanode.

reduce the travel distance of photogenerated holes, decreasing the chance of recombination. Secondly, p-Co_3O_4 OECs with interlaced nanosheets were dispersed on the surface of n-$BiVO_4$ for constructing heterojunctions,[8] enhancing charge separation by an internal electric field (IEF) and accelerate the kinetics of oxygen evolution reaction by the active site of cobalt. Lastly, the small particle size and high dispersion of Ag NPs accelerated interfacial electrons transport due to the formation of Schottky barrier, effectively improving the charge separation and greatly reducing the recombination of photogenerated electron hole pairs. Thus, highly efficient hamburger-like nanostructure of triadic $Ag/Co_3O_4/BiVO_4$ photoanode was fabricated, as illustrated in Fig. 1. Considering that the loading amount would change the size or morphology of Co_3O_4 OECs, the effects of Co_3O_4 loading amount on PEC performance for $Co_3O_4/BiVO_4$ heterojunction photoanode are discussed in detail. A working mechanism was also proposed to understand the improved separation of the photogenerated carriers by energy band structure, and the accelerated kinetics of oxygen evolution reaction at the interface of ternary components. In conclusion, the novel hamburger-like nanostructure of triadic $Ag/Co_3O_4/BiVO_4$ photoanode designed in this work is proven to represent a highly effective pathway to improve the PEC conversion efficiency.

2. Experimental sections

2.1 Preparation of pristine $BiVO_4$ photoanode

The pristine $BiVO_4$ photoanode was prepared from a Bi metal precursor reported previously.[19] In a typical synthesis, a Bi metal

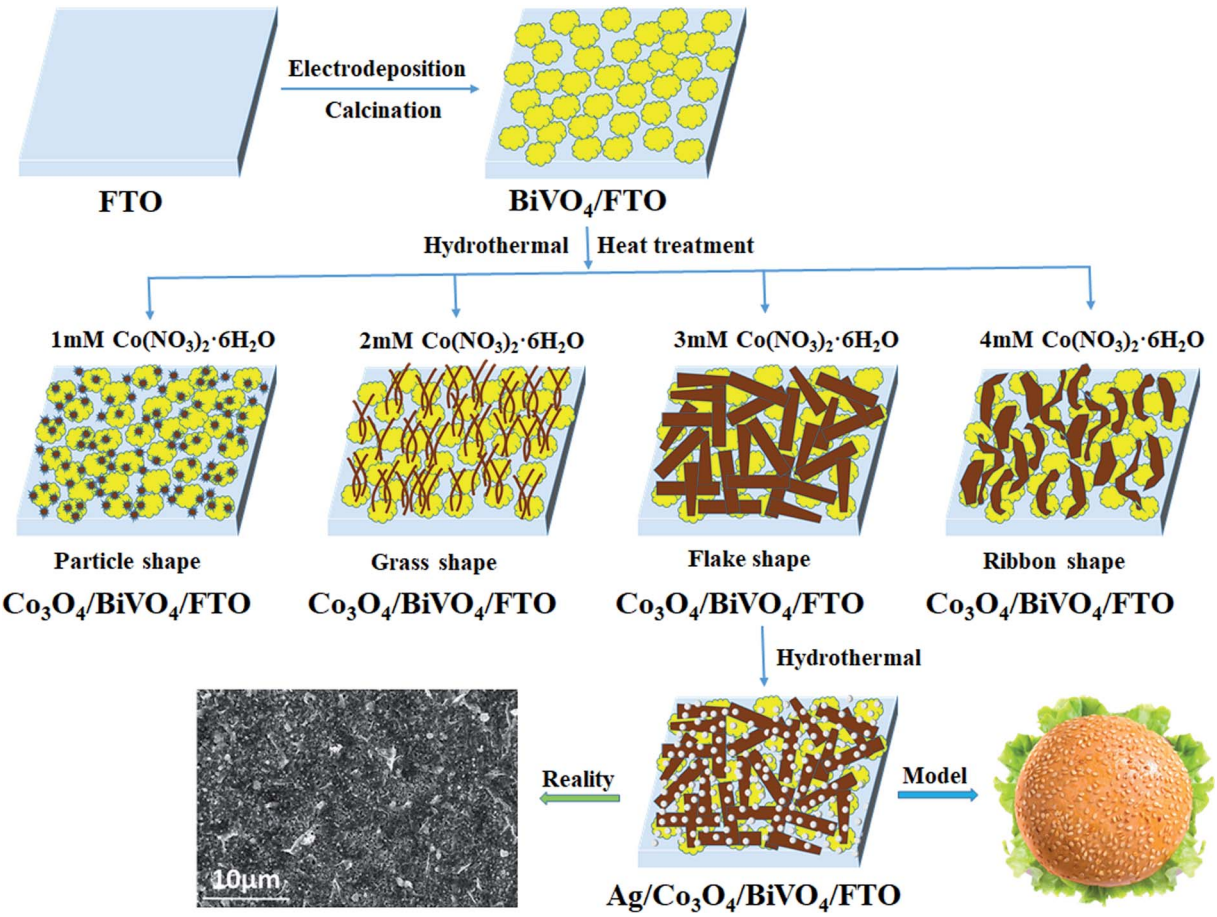

Fig. 2 Synthetic procedure of triadic $Ag/Co_3O_4/BiVO_4$ photoanode.

film was first electrodeposited in a three-electrode quartz cell system on the electrochemical workstation. Then the Bi metal film was converted into $BiVO_4$ after $VO(acac)_2$ DMSO solution were dipped onto the surface of the Bi metal film and heated at 450 °C for 2 h in air. Finally, the residual V_2O_5 was removed by 1 M NaOH solution. Thus, the $BiVO_4$ photoanode was obtained after washing and drying.

2.2 Preparation of $Co_3O_4/BiVO_4$ heterojunction photoanode

The $Co_3O_4/BiVO_4$ photoanode was fabricated after Co_3O_4 was loaded onto the surface of $BiVO_4$ photoanode by combing hydrothermal with heat treatment process. In order to investigate the effects of Co_3O_4 loading amount on PEC performance, the $Co_3O_4/BiVO_4$ photoanodes with different Co_3O_4 loading amount were prepared by adjusting the reactant concentration of Co precursor. Taking the optimal reactant concentration as an example, the $BiVO_4$/FTO substrates were transformed into Teflon-lined stainless steel autoclave containing 3 mM $Co(NO_3)_2 \cdot 6H_2O$, 10 mM NH_4F and 25 mM urea. The autoclave was sealed and maintained at 120 °C for 5 h and then cooled down to room temperature. The obtained composite photoanode was then calcined at optimum 350 °C for 3 h, thus the $Co_3O_4/BiVO_4$ photoanode was prepared accordingly. Similarly, the $Co_3O_4/BiVO_4$ photoanodes with different Co_3O_4 loading amount were prepared according to the $Co(NO_3)_2 \cdot 6H_2O$ concentration of 1 mM, 2 mM, 3 mM and 4 mM, keeping the concentration of 10 mM NH_4F and 25 mM urea unchangeably.

2.3 Preparation of $Ag/Co_3O_4/BiVO_4$ triadic photoanode

The FTO substrate coated with $Co_3O_4/BiVO_4$ heterojunction was immersed in a mixture solution containing 0.5 mM silver nitrate and 1 mM sodium citrate at 100 °C for 2 h. Afterwards, the $Ag/Co_3O_4/BiVO_4$ triadic photoanode[22] was rinsed with deionized water and dried in air. The complete synthesis process was sketched in Fig. 2. Additional details of chemicals, characterizations, PEC measurements and supporting data are available in ESI.†

3. Results and discussion

The phase composition of the samples was detected by XRD technique, and the corresponding results are shown in Fig. 3. In the XRD pattern of pure $BiVO_4$ photoanode (the red line), all diffraction peaks can be easily indexed to those of a monoclinic $BiVO_4$ cell (JCPDS No. 75-1866). The peaks at 2θ value of 19.00, 28.97 and 30.55 indexed to (011), (112) and (004) plane respectively, and no other crystalline phase like V_2O_5 or Bi_2O_3 was detected. Furthermore, it can be seen that weak diffraction peaks are consistent with cubic spinel Co_3O_4 phase (cell parameters: $a = 8.084$ Å; JCPDS No. 74-2120), as shown in the blue line. Even higher calcination temperature cannot improve the crystallinity of Co_3O_4 due to the low loading amount and high dispersion (Fig. S1†). Based on some experimental results and discussion (Fig. S2 and S3†), 350 °C was determined to the optimal calcining temperature for the formation of the $Co_3O_4/BiVO_4$ photoanode. After Ag NPs loading onto the $Co_3O_4/BiVO_4$/

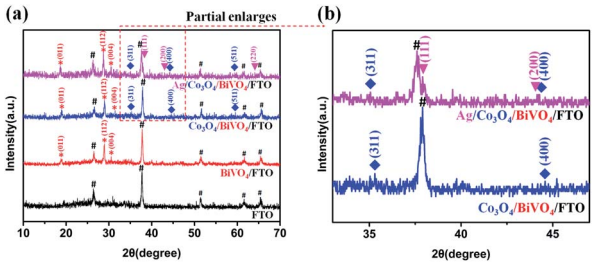

Fig. 3 (a) XRD patterns of FTO, $BiVO_4$/FTO, $Co_3O_4/BiVO_4$/FTO and $Ag/Co_3O_4/BiVO_4$/FTO. (b) Enlarged view of the area marked with the red dots in the (a) XRD patterns.

FTO, all monoclinic $BiVO_4$, cubic Co_3O_4 and Ag phases appeared simultaneously (the pink line in Fig. 3). In order to differentiate the lapped peaks of FTO and Ag NPs, the XRD patterns of 2θ values from 33 to 47 are enlarged partially. (111) and (200) with 2θ values around 38.11° and 44.30° preferred orientation diffraction peaks appeared, consistent with the crystal planes of metallic silver.

To further confirm the composition of the composite sample, XPS measurement was carried out as shown in Fig. 4. From the survey XPS spectrum (Fig. 4a), C 1s peak is located at 284.6 eV,[23] and except C, Bi, V, O, Co and Ag, no peaks of other elements could be observed, which indicates the presence of Co and Ag species on $BiVO_4$, compared with pristine $BiVO_4$. Fig. 4b and d present the high resolution XPS scan spectra of Bi 4f, V 2p, and O 1s. The Bi 4f XPS spectra in Fig. 4b show that the

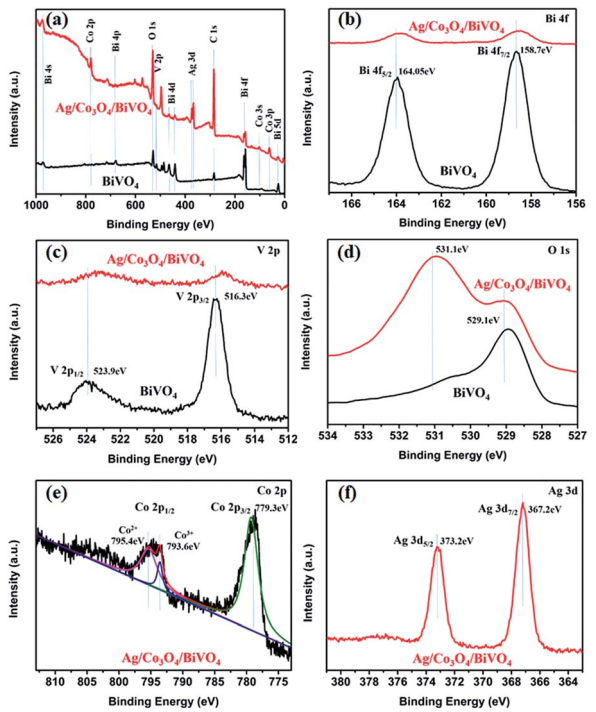

Fig. 4 XPS survey spectra of pristine $BiVO_4$ and $Ag/Co_3O_4/BiVO_4$: (a) survey scan; (b) Bi 4f; (c) V 2p; and (d) O 1s. (e) Co 2p and (f) Ag 3d scan spectra of $Ag/Co_3O_4/BiVO_4$.

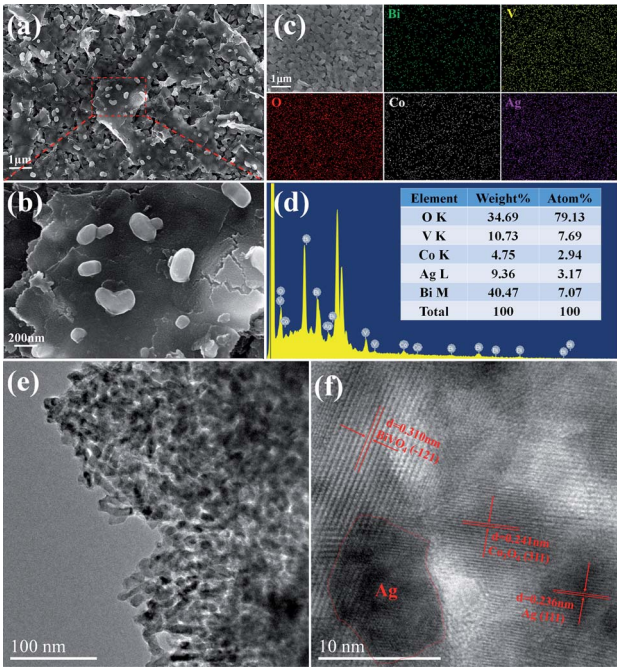

Fig. 5 SEM images (a and b) of Ag/Co_3O_4/$BiVO_4$, EDX mappings (c and d) for Ag/Co_3O_4/$BiVO_4$, TEM (e) and HRTEM (f) images of Ag/Co_3O_4/$BiVO_4$.

binding energies of Bi $4f_{7/2}$ and Bi $4f_{5/2}$ occur at 158.7 and 164.05 eV, respectively.[24] The V 2p peak in Fig. 4c can be fitted with two peaks at 523.9 and 516.3 eV, which are assignable to V $2p_{1/2}$ and V $2p_{3/2}$ signals, respectively.[25] Compared with the pure $BiVO_4$, an obvious negative shift in V 2p peaks and a slight negative shift in Bi 4f peaks are observed for Ag/Co_3O_4/$BiVO_4$, confirming the electron transfer from Co_3O_4 to $BiVO_4$.[26] At the same time, the O 1s spectra of pristine $BiVO_4$ and Ag/Co_3O_4/$BiVO_4$ shown in Fig. 4d exhibit the binding energies for O 1s (529.1 eV) core levels, while in the O 1s XPS spectrum of Ag/Co_3O_4/$BiVO_4$, a new peak (531.1 eV) appears as compared to pristine $BiVO_4$, which is probably caused by the Co loading and also indicates that the loaded Co species is exist in oxides form. The peaks located at 529.1 and 531.1 eV can be assigned to the oxygen species of lattice oxygen of layer-structured $Bi_2O_2^{2+}$ and Co_3O_4, respectively. The high-resolution spectrum for Co 2p (Fig. 4e) shows two major peaks with binding energies at 779.3 and 795.1 eV, corresponding to Co $2p_{3/2}$ and Co $2p_{1/2}$, respectively, which is the characteristic of a Co_3O_4. The spectra in the Co $2p_{1/2}$ region can be further deconvoluted into two peaks. The peaks at 793.6 eV and 795.4 eV are ascribed to Co^{3+} and Co^{2+} species respectively, which indicates the Co^{2+} and Co^{3+} species co-exist in the as-grown Co_3O_4 layer.[27] Fig. 4f shows that Ag 3d binding energies are 367.2 and 373.2 eV, confirming the existence of Ag.[28] Based on the XPS data, the examined sample was confirmed as Ag/Co_3O_4/$BiVO_4$ composite, and a strong interface interaction between photocatalyst $BiVO_4$ and cocatalyst Co_3O_4 would influence the resulting PEC properties, which will be discussed in later sections.

The morphology and microstructure of triadic Ag/Co_3O_4/$BiVO_4$ photoanode was characterized by FESEM and HRTEM in Fig. 5. The triadic Ag/Co_3O_4/$BiVO_4$ photoanode was fabricated by $BiVO_4$ nanobulks deposited with Co_3O_4 nanosheets and Ag nanoparticles as shown in Fig. 5a. It can be observed that $BiVO_4$ nanobulks were covered under the Co_3O_4 nanosheets, and Ag nanoparticles were evenly distributed on the surface of Co_3O_4 in Fig. 5b. The microstructure and elemental distribution of Ag/Co_3O_4/$BiVO_4$ are further revealed by the TEM and energy dispersive X-ray (EDX) mappings. EDX image of Ag/Co_3O_4/$BiVO_4$ photoanode indicates the presence of the Bi, V, Co, Ag and O (Fig. 5d). The elemental mappings of Fig. 5c display that the $BiVO_4$ nanobulks are well-distributed under Co_3O_4 nanosheets and Ag nanoparticles, and the EDX mapping analyses are consistent with the SEM observation. From TEM image in Fig. 5e, three components of the triadic photoanode were uniformly distributed. The HRTEM image in Fig. 5f shows the distinct lattice fringe of Ag/Co_3O_4/$BiVO_4$ complex. The fringes spacing is measured to be 0.310 nm, which corresponded to the (−121) lattice spacing of $BiVO_4$. In addition, the Co_3O_4 displays a lattice spacing of 0.241 nm, corresponding to the (311) plane.[8]

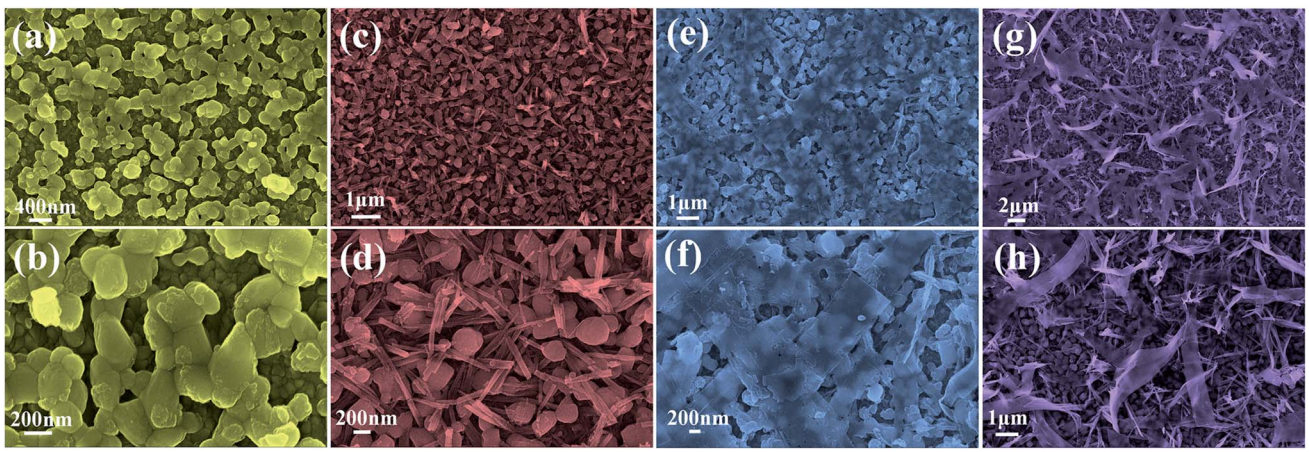

Fig. 6 SEM images (a and b) of 1 mM Co_3O_4/$BiVO_4$; (c and d) of 2 mM Co_3O_4/$BiVO_4$; (e and f) of 3 mM Co_3O_4/$BiVO_4$; (g and h) of 4 mM Co_3O_4/$BiVO_4$.

A typical lattice spacing of 0.236 nm indexed to (111) plane of Ag, revealing that the Ag nanoparticles were loaded on the Co_3O_4 nanosheets closely.[29]

To give a deep insight into the loading amount for changing the nanostructure of Co_3O_4 layer, the effects of Co_3O_4 loading on $BiVO_4$ photoanodes were further investigated by controlling the reactant concentration of $Co(NO_3)_2 \cdot 6H_2O$. As illustrated in Fig. 6, it is interesting to note that various nanostructured Co_3O_4 cocatalysts were obtained in the reaction solutions with different cobalt precursor concentrations. As shown in Fig. 6a and b, when the cobalt precursor was 1 mM, Co_3O_4 can only be dispersed in particle shape on $BiVO_4$ nanobulks. When the cobalt precursor concentration was adjusted to 2 mM, the one-dimensional Co_3O_4 nanowires with a diameter of ~50 nm in grass shape were obtained, as shown by the SEM images in Fig. 6c and d. When the cobalt precursor concentration continued to rise to 3 mM, the two-dimensional Co_3O_4 nanosheets in flake shape were observed in Fig. 6e and f, which are interwoven with each other and laid flat on $BiVO_4$ nanobulks. As illustrated in Fig. 6g and h, the solvothermal syntheses in the solutions with 4 mM cobalt precursor resulted in the growth of three-dimensional Co_3O_4 nanosheets in ribbon shape. The as-prepared $Co_3O_4/BiVO_4$ heterojunction photoanodes with different Co_3O_4 loading amount have obvious effects on PEC properties, which will be discussed in detail next.

The PEC measurements were achieved to disclose the functional roles of Co_3O_4 when coupled with $BiVO_4$ (Fig. 7). The current–voltage behaviors of the photoanodes under illumination and in the dark were studied as shown in Fig. 7a. In the dark, the current densities of the four photoanodes are almost zero, until the electrocatalytic oxidation peaks of cobalt appear at 0.95 V *vs.* Ag/AgCl. It can be observed that with the increase of Co_3O_4 loading amount, the electrocatalytic oxidation of water is stronger, that is, the peak strength increases and the onset potential shifts negatively. However, the difference is that 3 mM $Co_3O_4/BiVO_4$ heterojunction electrode has no obvious oxidation peak, which may be ascribed to highly dispersed Co^{2+}/Co^{3+} species oxidizing more easily to higher valence Co^{3+}/Co^{4+}, expediting the kinetics.[30] Under illumination, 3 mM $Co_3O_4/BiVO_4$ photoanode exhibited the highest photocurrent response, with the increase of Co_3O_4 loading amount. However, with the increase of excessive Co_3O_4 loading on 4 mM $Co_3O_4/BiVO_4$ photoanode, the corresponding light response is particularly poor, even shows no obvious response compared to the behaviour in the dark. Nevertheless, an in-depth investigation of the current–potential curves measured under chopped light illumination in Fig. 7b reveals that the 4 mM $Co_3O_4/BiVO_4$ photoanode is not nonresponsive but severely suppressed. When the photoanode was exposed to incident light, an anodic photocurrent spike was observed and then rapidly dropped to nearly zero, which is associated with the sudden generation of charge carriers and the subsequent recombination process.[31] Electrochemical impedance spectroscopy (EIS) studies were further carried out to investigate the charge transport behaviour at the electrode/electrolyte interface in these photoanodes. The obtained EIS data is fitted to an equivalent circuit shown in Fig. 7c, and the parameters extracted from the Nyquist fit are listed in Table S1.† R_s is defined as the series resistance, R_{ct1} in low impedance (high frequency) represents charge transfer resistance across the interface between the semiconductors, R_{ct2} in high impedance (low frequency) is the charge transfer resistance across the electrode/electrolyte interface.[32–34] A smaller semidiameter of the semicircle represents a better charge transfer ability (*i.e.*, faster surface reaction kinetics).[35] 4 mM $Co_3O_4/BiVO_4$ photoanode exhibited the largest semidiameter and the highest low-frequency impedance R_{ct2} in agreement with its worse PEC activity, which also suggests the severe aggregation and recombination of photogenerated carriers, rather than favourable migration to involve in water oxidation reaction.[32] 3 mM $Co_3O_4/BiVO_4$ photoanode presented the lowest low-frequency impedance R_{ct2} and the best PEC behaviour, which may be also attributed to its interlaced 2D nanosheet structure for facilitating the carrier transportation and surface water oxidation reaction. Current–potential curves of the 3 mM $Co_3O_4/BiVO_4$ photoanode under different illumination conditions are shown in Fig. 7d. The dark and light behaviours are very consistent with current–potential curve under chopped illumination upon turning on or off the light, but the sharp photocurrent spikes can still be clearly observed, which requires further improvement of its PEC performance. The above results indicate that the PEC properties of $Co_3O_4/BiVO_4$ composite photoanode are affected by the loading amount and nanostructure of Co_3O_4 layer.

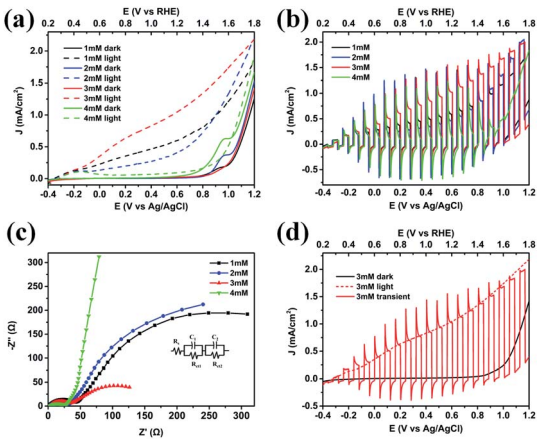

Fig. 7 (a) Current–voltage curves of the photoanodes under illumination (dashed line) and in the dark (solid line). (b) Current–potential curves of the photoanodes under chopped AM1.5G illumination. (c) Nyquist plots of the photoanodes under illumination. Inset: the corresponding equivalent circuit. (d) Current–potential curves of the 3 mM $Co_3O_4/BiVO_4$ photoanode under different illumination conditions. All measurements were taken in 0.1 M PBS solution.

Diffuse reflectance UV-visible spectra (DRS) were collected for $BiVO_4$, Co_3O_4 and $Co_3O_4/BiVO_4$ photoanodes to understand the influence of the heterostructure on light harvesting capability and to discuss the mechanism of charge separation for p-Co_3O_4/n-$BiVO_4$ heterojunction. As demonstrated in Fig. S4a,† pristine $BiVO_4$ photoelectrode shows a typical semiconductor absorption, whose absorption edge is located approximately at 500 nm. After loading the Co_3O_4 layer, the absorption edge of $Co_3O_4/BiVO_4$ obviously red-shifts and the absorption can be

significantly enhanced in the whole visible region, which implies that the Co_3O_4/$BiVO_4$ composite photoanode has better visible light absorption capacity. Moreover, it is not difficult to find that the trend of light absorption enhancement for p-Co_3O_4/n-$BiVO_4$ photoanode is very consistent with the light absorption characteristics of Co_3O_4 film, which is attributed to Co_3O_4 as a p-type semiconductor with narrower bandgap width. The direct band gap energy (E_g) of $BiVO_4$ and Co_3O_4 are evaluated to be 2.50 and 2.06 eV respectively, as shown in Fig. S4b.† The E_g of the composite photoanode is further narrowed to 2.0 eV, which suggests the formation of heterojunction with the strong interaction between n-$BiVO_4$ and p-Co_3O_4, consistent with the aforementioned XPS results. The band positions of pure $BiVO_4$ and Co_3O_4 before contact were predicted theoretically from the absolute electronegativity using eqn (1) and (2):

$$E_V = X - E_e + 0.5E_g \quad (1)$$

$$E_C = E_V - E_g \quad (2)$$

where E_C and E_V are conduction band (CB) and valence band (VB) positions, E_e is the energy of free electrons on the hydrogen scale (~4.5 eV), E_g is the bandgap and X is the absolute electronegativity of the semiconductor.[19] The X values for Co_3O_4 and $BiVO_4$ are 5.903 eV and 6.035 eV, respectively.[8,20] According to the estimated conduction, valence band edges, and E_g values of $BiVO_4$ and Co_3O_4, a mechanism of charge separation for p-Co_3O_4/n-$BiVO_4$ heterojunction is proposed as displayed in Fig. S4c.† In the heterostructure formed with p-Co_3O_4 and n-type semiconductors, there is a space charge region caused by the opposite direction diffusion of electrons in n-type semiconductors and holes in p-type semiconductors, leading to a p–n junction at the interface of semiconductors and an IEF from n-type semiconductors to p-type semiconductors. Then Fermi levels of p-type and n-type semiconductors must be identical at thermal equilibrium, forming a favorable band bending between $BiVO_4$ and Co_3O_4. On illumination as demonstrated, the photoexcited holes on the VB of $BiVO_4$ can transfer to Co_3O_4, while the electrons on the CB of Co_3O_4 transfer to $BiVO_4$ driven by an IEF at the Co_3O_4/$BiVO_4$ interface after contact. As a consequence, the photoexcited electrons and holes in the Co_3O_4/$BiVO_4$ heterostructure can be separated efficiently by the p–n junction due to the contrary direction of carrier migration. Furthermore, the sluggish surface reaction kinetics is overcome

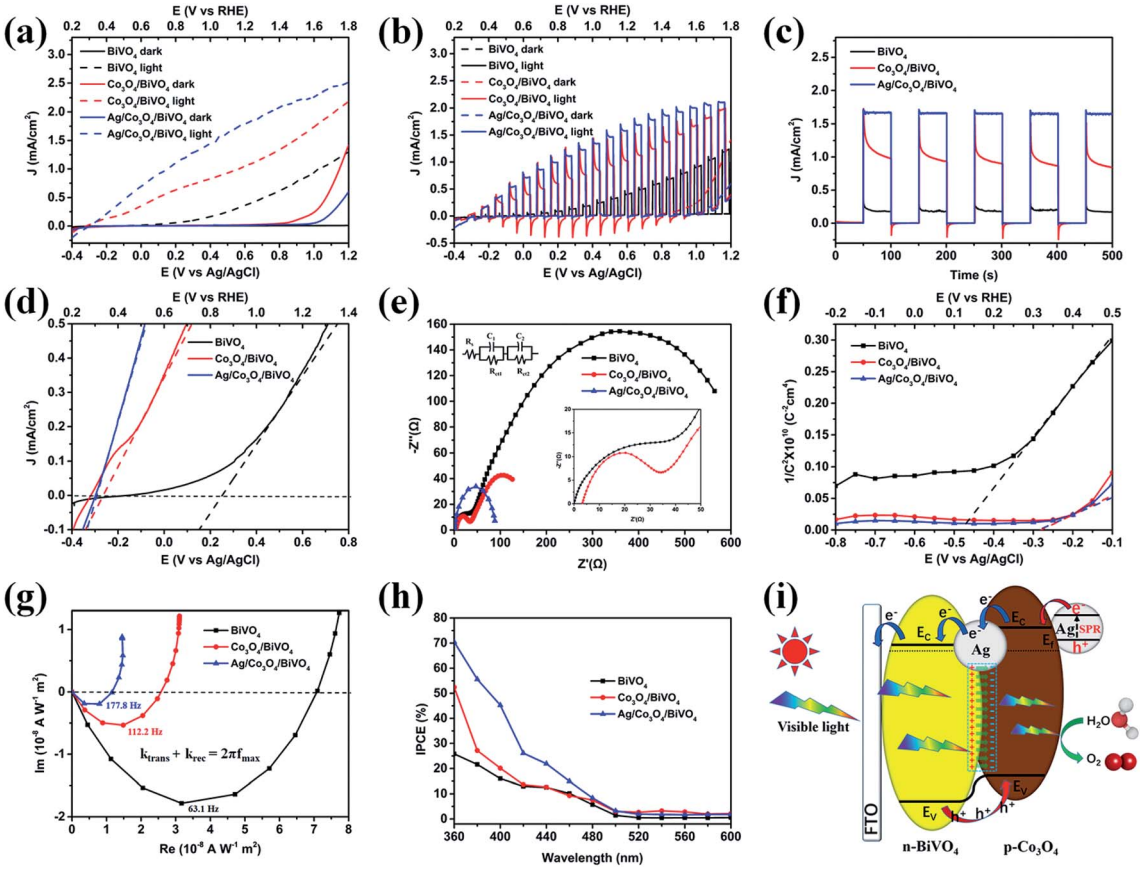

Fig. 8 (a) Current–voltage curves of the photoanodes under illumination (dashed line) and in the dark (solid line). (b) Current–potential curves of the photoanodes under chopped AM1.5G illumination. (c) Photocurrent–time curves at 1.23 V *vs.* RHE. (d) Enlarged image of current–voltage curves of the photoanodes under illumination (solid line). (e) EIS measured at 1.23 V *vs.* RHE under illumination. (f) Mott–Schottky plots collected at a frequency of 1 kHz in the dark. (g) Intensity-modulated photocurrent spectroscopy (IMPS) responses of the photoanodes. (h) The IPCE measured at 1.23 V *vs.* RHE under monochromatic light irradiation. (i) A schematic illustration for the PEC water oxidation process over the triadic Ag/Co_3O_4/$BiVO_4$ photoanode. All measurements were taken in 0.1 M PBS solution.

by the Co_3O_4 OECs, which further lowers the overpotential for water oxidation.

Although the as-prepared $Co_3O_4/BiVO_4$ heterojunction photoanode has played a good role in charge separation, carrier transport is still not ideal, as can be seen from the transient current curve in Fig. 7d. Considering the excellent electron conductivity and catalytic performance of silver nanoparticles, we tried to further improve the PEC performance of composite photoanode by loading Ag NPs. As shown in Fig. 8a, pristine $BiVO_4$ photoanode displays a relatively low photoresponse with a photocurrent density of 0.40 mA cm^{-2} at 1.23 V *vs.* RHE. A largely enhanced photocurrent density (1.08 mA cm^{-2}) is observed for the $Co_3O_4/BiVO_4$ heterojunction photoanode. In the case of triadic $Ag/Co_3O_4/BiVO_4$ photoanode, the photocurrent density further reaches to 1.84 mA cm^{-2} at 1.23 V *vs.* RHE, 4.60 and 1.70 times higher than that of the pristine $BiVO_4$ and $Co_3O_4/BiVO_4$ samples, respectively. Moreover, the photoconversion efficiency (PCE) of each photoanode was calculated based on the photocurrent response as shown in Fig. S5.† The PCE of triadic $Ag/Co_3O_4/BiVO_4$ photoanode reached 0.483% at 0.7 V *vs.* RHE, 28.4 times higher than the pristine $BiVO_4$ (0.017%) and 1.8 times higher than $Co_3O_4/BiVO_4$ photoanode (0.267%). In addition, Fig. 8b shows the transient photocurrent response of the photoanodes under chopped light illumination. The instantaneous current when the light is switched ON is a measure of the flux of holes into the surface. The subsequent decay towards the steady state current results from the capture of build-up holes in surface states inducing an electron flux associated with recombination.[36] In particular, the cathodic current overshoot observed when the light is switched OFF is due to the continuing flux of electrons from Co_3O_4 into the surface, correspondingly, no cathodic current was observed in the pristine $BiVO_4$ photoanode. When Ag NPs were loaded onto the surface of Co_3O_4, and interlayers between Co_3O_4 and $BiVO_4$, the surface plasma resonance (SPR) effect and excellent electrical conductivity of Ag NPs inhibited the recombination of surface electrons and holes, which further improved the photocurrent response.[37] The effect of Ag NPs was further confirmed by the chronoamperometry measurement under chopped light illumination in Fig. 8c. Amperometric *I–t* curves also depict the fast response toward irradiation stimulation in five cycles of switching light ON and OFF. The current density of these electrodes under illumination follows a descending order as: $Ag/Co_3O_4/BiVO_4$ > $Co_3O_4/BiVO_4$ > pristine $BiVO_4$. This is in high accordance with the LSV results (Fig. 8a) and further demonstrates the improvement in PEC performance provided by Co_3O_4 and Ag NPs. Moreover, the square profiles and steady photocurrent density of transient photocurrent response in $Ag/Co_3O_4/BiVO_4$ indicate a fast surface oxidation kinetics, suppressed electron–hole recombination and excellent photochemical stability.[38] Fig. 8d shows an enlarged image of the current–voltage performance of the photoanodes under illumination based on Fig. 8a. Compared to pristine $BiVO_4$, the onset potential of the $Co_3O_4/BiVO_4$ heterojunction significantly reduces from 0.86 V to 0.35 V with a cathodic shift of 510 mV. This cathodic shift value is the highest amongst all reported ones, in which $BiVO_4$ photoanodes were composited with a p-type semiconductor Co_3O_4, NiO or WO_3.[8,39–41] Furthermore, the onset potential is further negatively shifted 40 mV after modification of Ag NPs. The above results indicate that the triadic $Ag/Co_3O_4/BiVO_4$ photoanode further inhibited the electron–hole recombination and enhanced the photoresponse, after Ag NPs were introduced into the p-Co_3O_4/n-$BiVO_4$ heterojunction.

To gain further insight into the mechanism of the triadic $Ag/Co_3O_4/BiVO_4$ photoanode, the charge transfer at the photoanodes and water oxidation kinetics at the photoanode/electrolyte interface are evaluated using EIS plots. As shown in Fig. 8e, the obtained EIS data is fitted to an equivalent circuit,[32–34] and the parameters are listed in Table S2.† As reported, the first arc (high frequency) represents the charge transfer step and the second arc (low frequency) corresponds to the surface water oxidation step.[26] Compared to the pristine $BiVO_4$ photoanode, $Co_3O_4/BiVO_4$ photoanode exhibits smaller diameter of both two arcs, indicating that Co_3O_4 can boost the charge separation/transfer and surface reaction kinetics simultaneously, which can be attributed to the formation of $Co_3O_4/BiVO_4$ p–n junction and great catalytic activity of Co_3O_4 cocatalysts toward water oxidation. After introducing Ag NPs, the semicircle in the high-frequency region is eliminated and the semicircle in the low-frequency region is further reduced, indicating that the triadic $Ag/Co_3O_4/BiVO_4$ photoanode has better charge separation and transportation performance. Moreover, the flat band potential is obtained by extrapolating the Mott–Schottky plot to $1/C^2 = 0$ (Fig. 8f). Compared to the pristine $BiVO_4$, an evidently positive shift is observed for the $Co_3O_4/BiVO_4$ photoanode. The positive shift of the flat band potential for $Co_3O_4/BiVO_4$ suggests a decrease in the band bending, thus facilitating electrode/electrolyte interface charge transfer.

Intensity modulated photocurrent spectroscopy (IMPS) is a useful method to study semiconductor charge transport properties and is widely used in electron transport characterization of PEC devices.[42] Fig. 8g shows typical IMPS responses of pristine $BiVO_4$, $Co_3O_4/BiVO_4$ and $Ag/Co_3O_4/BiVO_4$ photoanodes in the complex plane. The semicircle observed in the fourth quadrant provides information on the combination of charge transfer and relaxation inside the photoanode.[43] Accordingly, the frequency of the maximum imaginary corresponds to the sum of the charge transfer (k_{trans}) and recombination (k_{rec}) rate constants ($k_{trans} + k_{rec} = 2\pi f_{max}$). The transient time of the electron (τ_d) was calculated according to the characteristic frequency apex of IMPS imaginary components. According to Fig. 8g, τ_d values of $BiVO_4$, $Co_3O_4/BiVO_4$ and $Ag/Co_3O_4/BiVO_4$ were calculated to be 2.52, 1.42 and 0.90 ms, respectively. This result indicates that the $Co_3O_4/BiVO_4$ photoanode has a higher electron transfer rate than that of pristine $BiVO_4$ photoanode, which results from band bending at the interface in heterojunction, leading to a directional flow of electron. The time constant further decrease to 0.90 ms for Ag NPs modified $Co_3O_4/BiVO_4$ photoanode, indicating the enhanced carries transport and better surface reaction kinetics for water oxidation, which supports the EIS and Mott–Schottky results very well. The incident photon-to-current efficiency (IPCE) value is

a critical index to study solar energy conversion efficiency. The $Co_3O_4/BiVO_4$ photoanode presents a higher IPCE value than $BiVO_4$ from UV extending to the visible region (Fig. 8h). Moreover, the $Ag/Co_3O_4/BiVO_4$ has higher IPCE profile than that of $Co_3O_4/BiVO_4$ until 500 nm, which is attributed to their corresponding SPR absorption peaks in the visible region.[38] This SPR wavelength dependent IPCE feature signifies that excitation of the Ag SPR is also responsible for the improved PEC performance of the triadic $Ag/Co_3O_4/BiVO_4$ photoanode. As a consequence, the IPCE value of ternary photoanode at 400 nm is up to 45.3%, which is 2.83 and 2.25 times higher than that of $BiVO_4$ and $Co_3O_4/BiVO_4$ respectively. The largely enhanced IPCE of the triadic $Ag/Co_3O_4/BiVO_4$ photoanode further confirms the integrated contribution of Co_3O_4 layer and Ag NPs to the PEC performance.

Given the discussion above, a mechanism for the enhanced PEC water oxidation performance in this triadic $Ag/Co_3O_4/BiVO_4$ photoanode is proposed and shown in Fig. 8i. Firstly, $BiVO_4$ with a small bandgap can utilize a significant portion of visible light to generate electrons and holes, and its valence band (VB) edge is positive enough to provide the holes with sufficient overpotential for the water oxidation reaction. When p-Co_3O_4 and n-$BiVO_4$ come into contact, a p–n junction is formed at their interface. Then the photoexcited holes on the VB of $BiVO_4$ can transfer to Co_3O_4, while the electrons on the CB of Co_3O_4 transfer to $BiVO_4$ that is driven by an IEF at the $Co_3O_4/BiVO_4$ interface. Furthermore, the unique interwoven nanostructure composed of 2D Co_3O_4 nanosheets could shorten the hole diffusion distance and facilitate the transport of holes to the surface. Besides, the highly dispersed Co^{2+}/Co^{3+} species within the Co_3O_4 ultrathin nanosheets can be oxidized to higher valence Co^{3+}/Co^{4+}, which are believed to catalyse water oxidation and expedite the kinetics. Finally, the interlaminar Ag induced surface potential at $Co_3O_4/BiVO_4$ interface facilitates rapid carrier separation and transport.[44] Meanwhile, under the irradiation of simulated solar light, the hot electrons generated by the SPR effect of Ag NPs can transfer to the conduction band (CB) of Co_3O_4.[37,45] Then the oscillation of the Ag NPs facilitates electron movement from Co_3O_4 to $BiVO_4$ and improves the photocurrent response.[37] Besides, the Schottky barrier existing at the interface of Ag and Co_3O_4 can efficiently prevent the hot electrons accumulated in Co_3O_4 from returning back to Ag nanoparticles, which is confirmed by the XPS and IPCE results.[45,46] Consequently, the significant enhancement in PEC performance of the triadic $Ag/Co_3O_4/BiVO_4$ photoanode can be ascribed to the 2D structure/p–n junction/SPR effect triple functionality.

4. Conclusions

The work demonstrates that the novel hamburger-like nanostructure of triadic $Ag/Co_3O_4/BiVO_4$ photoanode based on ingenious design is successfully prepared, where the Co_3O_4 plays a synergistic role of OECs and p–n heterojunction, meanwhile Ag NPs enhance carrier transport and inhibit electron–hole recombination due to the SPR effect. The resulting ternary photoanode exhibit significantly enhanced efficiency in PEC water splitting: the photocurrent density enhances 4.60 times than pristine $BiVO_4$ and higher than other $BiVO_4$ composites reported in literatures. The IPCE of $Ag/Co_3O_4/BiVO_4$ reaches 2.83 times higher than $BiVO_4$ due to the charge transit time shorten trebly than $BiVO_4$ from IMPS spectra. The onset potential of the ternary well-constructed photoanode has an astonishing cathodic shift of 550 mV compared to the pristine $BiVO_4$ photoanode. Besides, the positive shift of flat band potential, the enhancement of carrier density and the decrease in energy gap are also driven by synergistic action of p–n junction and SPR effect. It is expected that this strategy can be extended to other multilevel heterostructures for advanced performance in the fields of energy conversion and storage.

Conflicts of interest

There are no conflicts to declare.

Acknowledgements

This work was supported by the Central University Basic Scientific Research Operating Expenses Project and National College Student Innovation and Entrepreneurship Training Program from Beijing University of Chemical Technology.

References

1 Y. Cui, L. Pan, Y. Chen, N. Afzal, S. Ullah, D. Liu, L. Wang, X. Zhang and J.-J. Zou, *RSC Adv.*, 2019, **9**, 5492–5500.
2 M. G. Lee, D. H. Kim, W. Sohn, C. W. Moon, H. Park, S. Lee and H. W. Jang, *Nano Energy*, 2016, **28**, 250–260.
3 S. Kumar, S. Ahirwar and A. K. Satpati, *RSC Adv.*, 2019, **9**, 41368–41382.
4 J. Liu, S.-M. Xu, Y. Li, R. Zhang and M. Shao, *Appl. Catal., B*, 2020, **264**, 118540.
5 W. Jiang, Y. Jiang, J. Tong, Q. Zhang, S. Li, H. Tong and L. Xia, *RSC Adv.*, 2018, **8**, 41439–41444.
6 S. J. A. Moniz, S. A. Shevlin, D. J. Martin, Z.-X. Guo and J. Tang, *Energy Environ. Sci.*, 2015, **8**, 731–759.
7 J. Qi, D. Kong, D. Liu, L. Pan, Y. Chen, X. Zhang and J.-J. Zou, *RSC Adv.*, 2019, **9**, 15629–15634.
8 X. Chang, T. Wang, P. Zhang, J. Zhang, A. Li and J. Gong, *J. Am. Chem. Soc.*, 2015, **137**, 8356–8359.
9 J. Liu, J. Li, M. Shao and M. Wei, *J. Mater. Chem. A*, 2019, **7**, 6327–6336.
10 S. Byun, G. Jung, S.-Y. Moon, B. Kim, J. Y. Park, S. Jeon, S.-W. Nam and B. Shin, *Nano Energy*, 2018, **43**, 244–252.
11 K. Okuno, H. Kato, J. J. M. Vequizo, A. Yamakata, H. Kobayashi, M. Kobayashi and M. Kakihana, *RSC Adv.*, 2018, **8**, 38140–38145.
12 J. H. Kim and J. S. Lee, *Adv. Mater.*, 2019, **31**, 1806938.
13 C. Ràfols i Bellés, S. Selim, N. M. Harrison, E. A. Ahmad and A. Kafizas, *Sustainable Energy Fuels*, 2019, **3**, 264–271.
14 T. W. Kim and K.-S. Choi, *Science*, 2014, **343**, 990.
15 S. Wang, T. He, J.-H. Yun, Y. Hu, M. Xiao, A. Du and L. Wang, *Adv. Funct. Mater.*, 2018, **28**, 1802685.

16 Y. Hermans, S. Murcia-López, A. Klein, R. van de Krol, T. Andreu, J. R. Morante, T. Toupance and W. Jaegermann, *Phys. Chem. Chem. Phys.*, 2019, **21**, 5086–5096.
17 X. Zhao, W. Luo, J. Feng, M. Li, Z. Li, T. Yu and Z. Zou, *Adv. Energy Mater.*, 2014, **4**, 1301785.
18 Z.-F. Huang, L. Pan, J.-J. Zou, X. Zhang and L. Wang, *Nanoscale*, 2014, **6**, 14044–14063.
19 S. Bai, J. Liu, M. Cui, R. Luo, J. He and A. Chen, *Dalton Trans.*, 2018, **47**, 6763–6771.
20 J. Wang and F. E. Osterloh, *J. Mater. Chem. A*, 2014, **2**, 9405–9411.
21 C.-C. Hou, T.-T. Li, Y. Chen and W.-F. Fu, *ChemPlusChem*, 2015, **80**, 1465–1471.
22 Y. Tang, R. Wang, Y. Yang, D. Yan and X. Xiang, *ACS Appl. Mater. Interfaces*, 2016, **8**, 19446–19455.
23 S. Bai, J. Liu, J. Guo, R. Luo, D. Li, Y. Song, C. C. Liu and A. Chen, *Sens. Actuators, B*, 2017, **249**, 22–29.
24 P. Guan, H. Bai, F. Wang, H. Yu, D. Xu, B. Chen, T. Xia, W. Fan and W. Shi, *ChemCatChem*, 2018, **10**, 4927–4933.
25 B. He, Y. Wang, X. Liu, Y. Li, X. Hu, J. Huang, Y. Yu, Z. Shu, Z. Li and Y. Zhao, *J. Mater. Chem. A*, 2019, **7**, 6747–6752.
26 R. Zhang, M. Shao, S. Xu, F. Ning, L. Zhou and M. Wei, *Nano Energy*, 2017, **33**, 21–28.
27 X. Dang, X. Zhang, X. Dong, W. Ruan, H. Ma and M. Xue, *RSC Adv.*, 2014, **4**, 54655–54661.
28 W. Zhao, J. Zhang, F. Zhu, F. Mu, L. Zhang, B. Dai, J. Xu, A. Zhu, C. Sun and D. Y. C. Leung, *Chem. Eng. J.*, 2019, **361**, 1352–1362.
29 T. Hong, Z. Liu, X. Zheng, J. Zhang and L. Yan, *Appl. Catal., B*, 2017, **202**, 454–459.
30 W. He, R. Wang, L. Zhang, J. Zhu, X. Xiang and F. Li, *J. Mater. Chem. A*, 2015, **3**, 17977–17982.
31 Y. Zhu, J. Ren, X. Yang, G. Chang, Y. Bu, G. Wei, W. Han and D. Yang, *J. Mater. Chem. A*, 2017, **5**, 9952–9959.
32 G. Liu, Y. Zhao, K. Wang, D. He, R. Yao and J. Li, *ACS Sustainable Chem. Eng.*, 2018, **6**, 2353–2361.
33 S. S. M. Bhat, S. A. Lee, T. H. Lee, C. Kim, J. Park, T.-W. Lee, S. Y. Kim and H. W. Jang, *ACS Appl. Energy Mater.*, 2020, **3**, 5646–5656.
34 X. Zhang, X. Wang, X. Yi, J. Ye and D. Wang, *ACS Sustainable Chem. Eng.*, 2019, **7**, 5420–5429.
35 B. Klahr, S. Gimenez, F. Fabregat-Santiago, T. Hamann and J. Bisquert, *J. Am. Chem. Soc.*, 2012, **134**, 4294–4302.
36 C. Y. Cummings, F. Marken, L. M. Peter, A. A. Tahir and K. G. U. Wijayantha, *Chem. Commun.*, 2012, **48**, 2027–2029.
37 Y. Ren, Q. Xu, X. Zheng, Y. Fu, Z. Wang, H. Chen, Y. Weng and Y. Zhou, *Appl. Catal., B*, 2018, **231**, 381–390.
38 F. Ning, M. Shao, S. Xu, Y. Fu, R. Zhang, M. Wei, D. G. Evans and X. Duan, *Energy Environ. Sci.*, 2016, **9**, 2633–2643.
39 M. Zhong, T. Hisatomi, Y. Kuang, J. Zhao, M. Liu, A. Iwase, Q. Jia, H. Nishiyama, T. Minegishi, M. Nakabayashi, N. Shibata, R. Niishiro, C. Katayama, H. Shibano, M. Katayama, A. Kudo, T. Yamada and K. Domen, *J. Am. Chem. Soc.*, 2015, **137**, 5053–5060.
40 L. Li, X. Yang, Y. Lei, H. Yu, Z. Yang, Z. Zheng and D. Wang, *Chem. Sci.*, 2018, **9**, 8860–8870.
41 S. S. Kalanur, I.-H. Yoo, J. Park and H. Seo, *J. Mater. Chem. A*, 2017, **5**, 1455–1461.
42 J. Su, L. Guo, N. Bao and C. A. Grimes, *Nano Lett.*, 2011, **11**, 1928–1933.
43 F. Yu, F. Li, T. Yao, J. Du, Y. Liang, Y. Wang, H. Han and L. Sun, *ACS Catal.*, 2017, **7**, 1868–1874.
44 X. Zhang, Y. Li, J. Zhao, S. Wang, Y. Li, H. Dai and X. Sun, *J. Power Sources*, 2014, **269**, 466–472.
45 S. Kim, Y. Yu, S. Y. Jeong, M. G. Lee, H. W. Jeong, Y. M. Kwon, J. M. Baik, H. Park, H. W. Jang and S. Lee, *Catal. Sci. Technol.*, 2018, **8**, 3759–3766.
46 C. Clavero, *Nat. Photonics*, 2014, **8**, 95–103.